

# Reaching the quantum noise limit for interferometric measurement of optical nonlinearity in vacuum

A. Aras,<sup>1,\*</sup> A. E. Kraych,<sup>1</sup> X. Sarazin,<sup>1</sup> E. Baynard,<sup>1</sup> F. Couchot,<sup>1</sup> and M. Pittman<sup>1</sup>

<sup>1</sup>Université Paris-Saclay, CNRS/IN2P3, IJCLab, 91405 Orsay, France

## Abstract.

Quantum Electrodynamics predicts that the vacuum must behave as a nonlinear optical medium: the vacuum optical index should increase when vacuum is stressed by intense electromagnetic fields. The DeLLight (Deflection of Light by Light) project aims to measure it by using intense and ultra-short laser pulses delivered by the LASERIX facility at IJCLab (Paris-Saclay University). The principle is to measure by interferometry the deflection of a low-intensity probe pulse when crossing the vacuum optical index gradient produced by an external high-intensity pump pulse. The detection of the expected signal requires measuring the position of the interference intensity profile with a high spatial resolution, limited by the ultimate quantum noise. However, the spatial resolution is highly degraded by the phase noise induced by the mechanical vibrations of the interferometer. In order to suppress this interferometric phase noise, we have developed a new method, named High-Frequency Phase Noise Suppression (HFPNS) method, based on the use of a delayed reference signal to correct any noise-related signal appearing in the probe beam. In this work, we present the experimental validation of this novel method. The results demonstrate a robust path toward picometer-scale sensitivity and provide a key step toward the observation of QED-induced vacuum refraction.

## I. INTRODUCTION

Classical electrodynamics treats the vacuum as a simple, passive, and empty space. Therefore, the Maxwell's equations are written linear in a vacuum preventing any interactions between electromagnetic fields. It is characterized by two universal constants: the electric permittivity  $\epsilon_0$  and the magnetic permeability  $\mu_0$ . The speed of light,  $c$ , which is directly related to those quantities  $\epsilon_0$  and  $\mu_0$ , is also a universal constant.

In contrast, Quantum Electrodynamics (QED) proposes the concept of a dynamic vacuum, where virtual particle-antiparticle pairs are constantly created and annihilated due to quantum fluctuations. The presence of virtual charged particles makes *light-by-light* interaction possible. In the presence of external electromagnetic fields, the vacuum should then behave as a nonlinear optical medium, leading to a decrease of the speed of light in vacuum. This phenomenon was first predicted by Euler and Heisenberg [1, 2], and later formulated within the QED framework by Schwinger [3] as photon-photon scattering.

From a corpuscular perspective, photon-photon scattering has already been observed in several experiments, firstly at the Stanford Linear Accelerator Center (SLAC) [4] with real photons and later at the Large Hadron Collider (LHC) [5, 6] with quasi-real photons. In these cases, the vacuum appears only in the virtual electron-positron pair exchange, but its fundamental electromagnetic properties remain unchanged, i.e. no modification of the vacuum electromagnetic constants  $\epsilon_0$ ,  $\mu_0$ , and  $c$ .

However, the optical nonlinearity in vacuum, a pure classical undulatory process with a modification of the

light velocity at macroscopic scale, has never been observed due to the need for ultra high electric or magnetic fields, as well as ultra-sensitive measurement techniques. The experimental efforts on this scope focus mainly on testing vacuum magnetic birefringence in the presence of an external magnetic field [7, 8]. The best sensitivity reached so far has been achieved by the PVLAS experiment, measuring the vacuum magnetic birefringence 7 times higher than the expected QED signal (in  $1\sigma$  confidence level), after 100 days of collected data [9]. New birefringence projects have been proposed in the recent years to CERN and XFEL to improve the sensitivity [10, 11].

The DeLLight experiment is an ongoing experiment designed to measure for the first time the optical nonlinearity of the vacuum by using ultra-intense femtosecond laser pulses delivered by the LASERIX facility at IJCLab (Paris-Saclay University). The experimental method involves measuring the refraction of a low-intensity probe laser pulse after crossing a vacuum optical index gradient imprinted by its nonlinear interaction with an external intense pump laser pulse. Because the QED-predicted deflection is extremely small, a Sagnac interferometer is employed to amplify the deflection signal. In the initial phase, the proof of concept of the DeLLight experiment was achieved by measuring the deflection of light by light in air, with low-intensity external pump pulses, demonstrating the amplification of the deflection signal through interferometric measurement [12, 13].

In addition to the signal amplification, the detection of the QED deflection signal in vacuum requires measuring the barycenter position of the interference signal with high spatial accuracy. However, the spatial resolution is highly limited by the phase noise induced by mechanical vibrations of the interferometer. In order to suppress the vibrational phase noise, we have developed a novel method, named High-Frequency Phase Noise Suppres-

\* ali.aras@ijclab.in2p3.fr

sion (HFPNS), which consists of splitting the incident probe laser pulse before entering the interferometer, into two identical pulses, one being delayed by few nanoseconds. The delayed pulse is then used to monitor and suppress the off-line interferometric phase noise considering the interferometric noise being the same for both the prompt and delayed pulses.

In this article, we first present the DeLLight experiment and the interferometric amplification method, detailing the different origins of noise limiting the spatial resolution. We then explain the HFPNS method, and describe the experimental setup developed to test and validate the method. Finally, the results are presented, demonstrating the complete suppression of the vibration phase noise within the current prototype along with the off-line data analysis procedure.

## II. DELLIGHT EXPERIMENT

### A. Interferometric measurement

The DeLLight interferometric method to measure the deflection of a probe laser pulse by an intense pump laser pulse is as follows, and schematized in Figure 1. A low-intensity laser pulse, of intensity  $I_{in}$ , is sent into a Sagnac interferometer via a 50/50 beamsplitter,  $BS$ , generating two daughter pulses (the probe and reference pulses) that circulate in opposite directions around the interferometer. Both pulses are focused via two optical lenses in the interaction area with a minimum waist at focus  $w_0$ .

The two counter-propagating pulses are in opposite phase in the dark output of the interferometer and interfere destructively. Due to the small asymmetry in reflection and transmission of the beamsplitter, the extinction of the interferometer is never total, and residual interference signal, of intensity  $I_{out}$ , is captured by a CCD camera in the dark output. The degree of extinction of the residual interference signal is characterized by the extinction factor  $\mathcal{F}$ , defined as  $\mathcal{F} = I_{out}/I_{in}$ .

The intense pump pulse of energy  $E_{pump}$  is now focused into the same interaction area with a minimum waist at focus  $W_0$ , in time coincidence and counter-propagating configuration with respect to the probe pulse. Its nonlinear coupling with the probe in vacuum generates an optical index gradient proportional to the intensity profile of the pump. The probe is then refracted due to this emergent index gradient by a deflection angle  $\delta\theta_{QED}$ , while the reference pulse is not in time coincidence with the pump and is therefore unaffected. After recollimation by the second lens, the refracted probe pulse is vertically shifted with respect to the unrefracted reference pulse by an average distance of  $\delta y_{QED} = f \times \delta\theta_{QED}$ , where  $f$  is the focal length.

As the deflected probe pulse interferes destructively with the unperturbed reference pulse, the transverse intensity profile of the interference signal in the dark output is then vertically shifted by a distance  $\Delta y_{QED}$ ,

which is amplified as compared to the direct would-be signal  $\delta y_{QED}$  obtained when using a standard pointing method [12].

The amplification factor, defined as  $\mathcal{A} = \Delta y_{QED}/\delta y_{QED}$ , scales as  $\mathcal{F}^{-1/2}$ . The greater the extinction is, the greater the amplified signal is. As studied in [13], the optimum extinction factor  $\mathcal{F} = 4 \times 10^{-6}$  has been experimentally demonstrated, corresponding to an amplification  $\mathcal{A} = 250$ . With the available energy of 2.5 J per pulses, delivered by the LASERIX facility, focused to  $W_0 = 5 \mu\text{m}$ , resulting in intensity on the order of  $2 \times 10^{20} \text{ W/cm}^2$ , the expected QED signal is  $\Delta y_{QED} \approx 15 \text{ pm}$ .

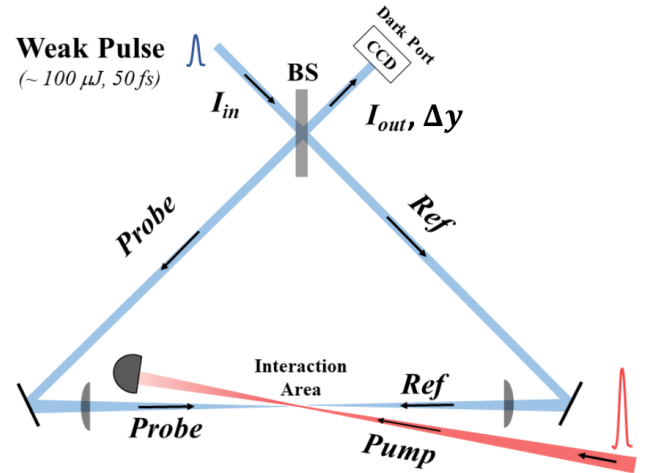


Figure 1. Sagnac interferometer layout with pump injection.

### B. Spatial resolution

The deflection signal is measured by alternating laser shots with and without interaction between the pump and the probe, referred to as “ON” and “OFF” measurements, respectively. For each laser shot, the resulting interference pattern is recorded by a CCD camera at the dark output of the interferometer. We extract the vertical barycenters of the interference intensity profile for successive ON and OFF measurements, which we name  $\bar{y}^{\text{ON}}(i)$  and  $\bar{y}^{\text{OFF}}(i)$ , respectively. The deflection signal  $\Delta y(i)$  of the  $i^{\text{th}}$  “ON-OFF” measurement, corresponding to a shift of the barycenter due to the interaction with the pump, is then defined as

$$\Delta y(i) = \bar{y}^{\text{ON}}(i) - \bar{y}^{\text{OFF}}(i). \quad (1)$$

The measured  $\Delta y(i)$  values have a certain distribution characterized by its mean value  $\langle \Delta y \rangle$  and its standard deviation  $\sigma_y$ , which we hereafter refer to as the *spatial resolution*. Collecting  $N$  ON-OFF measurements, the statistical error (one standard deviation) of the measured average value  $\langle \Delta y \rangle$  is then equal to  $\sigma_y/\sqrt{N}$ . So, regardless

the available intensity of the pump pulses at focus and the degree of extinction of the interferometer, the capacity of detecting the QED signal requires a large number of measurements  $N$ , but also, and above all, an excellent spatial resolution  $\sigma_y$ .

The spatial resolution is inherently limited by the intrinsic shot noise (quantum noise), related to the statistical fluctuations of the average number of photoelectrons detected by the CCD camera. As detailed in [14], the shot noise is independent of the beam width and it scales as  $d_{pix}/\sqrt{N_c}$ , where  $d_{pix}$  is the side length of each square pixels and  $N_c$  is the maximum number of detected photoelectrons per pixel before saturation, referred as the full well capacity of the CCD camera. As measured in [13], a spatial resolution of  $\sigma_y = 15$  nm can be obtained with the most appropriate commercial CCD camera. Assuming that the spatial resolution is only limited by the shot noise ( $\sigma_y = 15$  nm), and with the 10 Hz repetition rate of the LASERIX facility, the expected sensitivity at  $1\sigma$  confidence level to measure the QED signal could be reached after about 4 days of collected data.

However, significant beam pointing fluctuations are present, leading to fluctuations  $\delta y_{BP}$  of the barycenter of the intensity profile of the interference signal. Depending on the environmental conditions, these fluctuations are found on the order of a few micrometers which is three orders of magnitude larger than the shot noise. Such fluctuations induce at first order a global shift of the barycenter of the interference intensity profile.

As demonstrated in [13], when operating the interferometer without amplification, any pointing fluctuation of the interference signal can be monitored in real-time. By measuring its correlation with the back-reflection spots from the rear surface of the beamsplitter, which provides a direct image of the incident beam on the same CCD camera, these fluctuations are suppressed off-line.

In contrast, when the interferometer operates in the amplification regime, then the spatial resolution is significantly degraded by the emerging interferometric phase noise induced by mechanical vibrations of the interferometer. These vibrations produce a relative lateral displacement  $\delta y_\Phi$  between the two daughter pulses of interferometer, the probe and reference beams, in the dark output, leading to an amplified displacement  $\Delta y_\Phi$  of the interference intensity profile, and so an amplified noise by extension. In this regime, the barycenter of the interference intensity profile is no longer correlated to the one of the back-reflection. This noise becomes even dominant when increasing the RoI size, which is needed to reach a high efficiency as detailed in section IV.

It has been shown that the current level of vibrations must be reduced by two orders of magnitude in order to reach the ultimate shot noise spatial resolution [13]. It would need to develop a technically challenging and expensive mechanical system to reach an ultra-stable isolation level.

Here, an alternative method have been developed, named as High-Frequency Phase Noise Suppression (HF-

PNS), with the aim of measuring directly the displacement induced by the phase noise and after suppressing it off-line. It simply consists of splitting the incident probe laser pulse before entering the interferometer, into two identical pulses, one being delayed by few nanoseconds. Due to the small delay time, the vibration noise being the same for both the prompt and delayed pulses. The delayed pulse is then used to monitor and suppress off-line the interferometric phase noise. Details of the HFPNS method, description of the setup developed to demonstrate and validate the method and results are given in the next two sections, section III, and IV.

### III. HIGH FREQUENCY PHASE NOISE SUPPRESSION (HFPNS) METHOD

#### A. Description of the HFPNS Method

The optical setup of the HFPNS method is schematically shown in Figure 2. It consists of splitting the incident probe beam into two identical pulses. One pulse is transmitted directly, while the other one being delayed by about 5 ns using a delay line composed of two beam-splitters (BS-1 and BS-2) and two mirrors (M1 and M2).

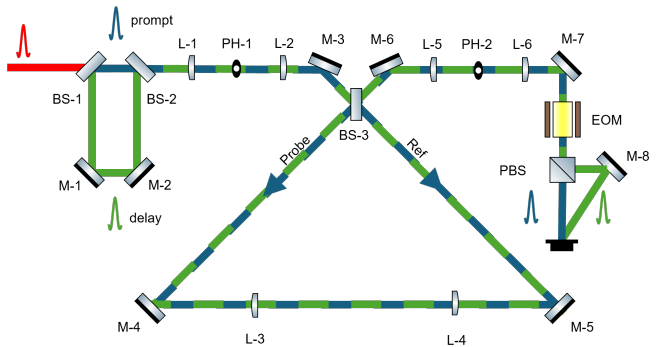


Figure 2. A simplified scheme of the optical design of DeLight experiment with HFPNS method setup.

The two time-separated beams are then directed to a spatial filter composed of a telescope of two lenses (L-1 and L-2) of same focal length 200 mm, and a pinhole (PH-1) with a diameter of 300  $\mu\text{m}$ , ensuring that they both have similar beam profile close to a Gaussian profile, before entering inside the Sagnac interferometer.

In the current HFPNS interferometer prototype, a 50/50 femtosecond p-pol beamsplitter BS-3 (Semrock FS01-BSTiS-5050P-25.5) is used to generate two daughter pulses, referred to as probe, and reference. The two dielectric mirrors (M-4 and M-5) are also positioned at 22.5° incident angle, forming a right-angle triangular interferometer. A telescope of two best form spherical lenses (L-3 and L-4) of focal length 100 mm (Thorlabs LBF254-100-B) is placed between these two mirrors in order to focus both pulses into the interaction area. The

incident beam waist is  $w \simeq 1$  mm, corresponding to a minimum waist  $w_0 \simeq 25\mu\text{m}$  at focus.

At the interferometer output, destructive interference pattern is separately obtained for both the prompt and delay pulses. Any scattered light from the interferometer is filtered by using a spatial filter consisting of a telescope with two 200 mm focal length lenses (L-5 and L-6) followed by a pinhole (PH-2) of 300  $\mu\text{m}$  diameter, ensuring a clean Gaussian intensity profile in the interferometer output.

Finally, an electro-optic modulator (EOM) (KD\*P Pockels Cell, Leysop Ltd) at 7.2kV is utilized in order to change the polarization of only the delay beam in high frequency (200 MHz) from pure p-state to s-state. The polarizing beamsplitter cube (PBS) is then used to separate spatially these two prompt and delay pulses from the same beamline. Finally, the output images are collected on the same CCD camera (Basler acA3088-16gm, pixel size  $5.84 \times 5.84 \mu\text{m}^2$ ) via a mirror (M-6). The efficiency of this separation on the CCD is measured by the intensity ratio of the delay beam on the prompt spot which is measured as 1:20.

Considering the small delay time of 5 ns, the phase noise induced by the vibrations inside the interferometer, and corresponding to the lateral shift  $\Delta y_\Phi$  of the interference intensity profiles, is then found identical for both the prompt  $I_{out}^P(y)$  and the delay  $I_{out}^D(y)$ , while both prompt and delay beams are affected by the same beam pointing fluctuations (neglecting the relative vibrations of the delay line), and are therefore correlated.

In contrast, thanks to their time coincidence, only the prompt pulse experiences the pump-induced deflection, which generates a shift  $\Delta y_{\text{QED}}$  in its interference intensity profile. The resulting intensity distributions for the prompt and delayed pulses can therefore be written as

$$I_{out}^P(y) = \mathcal{F} \times I_{in}(y + \Delta y_{BP} + \Delta y_\Phi + \Delta y_{\text{QED}}) \quad (2)$$

$$I_{out}^D(y) = \mathcal{F} \times I_{in}(y + \Delta y_{BP} + \Delta y_\Phi) \quad (3)$$

This configuration allows the delayed pulse to be used for the simultaneous measurement of beam pointing fluctuations and interferometric phase noise. Their contributions in the estimated barycenter, then, can be subtracted off-line in the analysis procedure, enabling the extraction of the pure QED-induced deflection signal  $\Delta y_{\text{QED}}$ .

## B. Extinction factor

A typical transverse intensity profile recorded by the CCD camera in the dark output of the HFPNS-interferometer is shown in Figure 3. The upper row of three spots corresponds to the prompt pulse, while the lower row represents the delay pulse. Within each row, the central spot corresponds to the interference signal. The two other spots observed on opposite lateral sides are due to back-reflections on the rear side of the beamsplitter. Their respective intensities are  $I_{AR,1} = I_{AR,2} =$

$(R_{AR}/2)I_{in}$ , where  $R_{AR} \simeq 10^{-3}$  is the back-reflection coefficient of the beamsplitter.

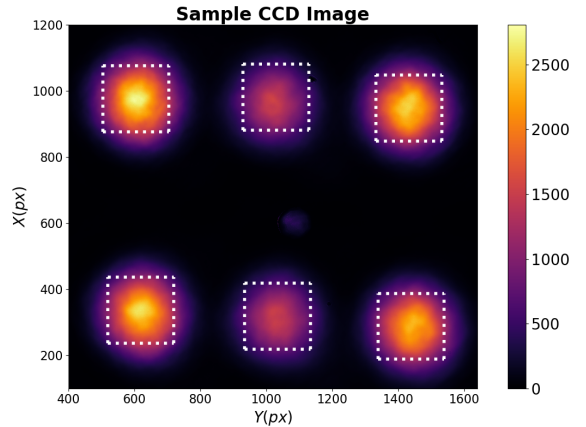


Figure 3. A CCD image of the intensity profiles of the prompt (top) and delay (bottom) probe pulses, recorded in the dark output of the interferometer. The interference signals is located in the central part. The two opposite lateral spots correspond to the back reflections on the rear side of the beamsplitter. The white dotted square areas correspond to the Region of Interest (RoI) used to calculate the barycenters.

In order to reach the ultimate spatial resolution high photons statistics is required in the interference signal intensity. This can be achieved by increasing the intensity of the incident pulse. However, with the currently available beamsplitter, the extinction factor becomes mainly limited by back-reflections, simply as saturating the CCD camera. To overcome this limitation, the extinction is adjusted such that the interference intensity is of the same order of magnitude as the back-reflection intensities. This tuning is obtained by slightly rotating the interferometer beamsplitter by about 1° in the horizontal plane, thereby changing the incident angle of the laser pulse from 45° to 46°. At this angle, the measured transmission and reflection coefficients are  $R \simeq 49\%$  and  $T \simeq 51\%$ , corresponding to an extinction factor  $\mathcal{F} = (\delta a)^2 \simeq 4 \times 10^{-4}$  and an amplification factor  $\mathcal{A} = 25$ , as measured in [12].

## C. Signal analysis method

For each successive CCD recorded image, a barycenter is calculated within a fixed square analysis window, defined as the Region of Interest (RoI) with width  $w_{\text{RoI}}$  (white dotted squares in Figure 3). This procedure is applied to both the prompt and the delayed interference intensity profiles, yielding barycenters  $\bar{y}_{P,\text{Sig}}^{\text{ON}}(i)$  and  $\bar{y}_{P,\text{Sig}}^{\text{OFF}}(i)$  for the prompt pulse, and  $\bar{y}_{D,\text{Sig}}^{\text{ON}}(i)$  and  $\bar{y}_{D,\text{Sig}}^{\text{OFF}}(i)$  for the delayed pulse, along the vertical axis, for each successive ON and OFF measurements.

To suppress the noise contributions on the calculated barycenter, we first determine the linear correlation be-

tween the prompt and delayed barycenters using only the OFF measurements. The resulting fit parameters,  $a_{\text{OFF}}$  and  $b_{\text{OFF}}$ , characterize the common noise shared by the two pulses. The corrected prompt signal positions are then obtained by subtracting this common noise through a linear regression-based procedure, given by:

$$\begin{aligned}\bar{y}_{\text{PD},\text{Sig}}^{\text{OFF}}(i) &= \bar{y}_{\text{P},\text{Sig}}^{\text{OFF}}(i) - (a_{\text{OFF}} \times \bar{y}_{\text{D},\text{Sig}}^{\text{OFF}}(i) + b_{\text{OFF}}) \\ \bar{y}_{\text{PD},\text{Sig}}^{\text{ON}}(i) &= \bar{y}_{\text{P},\text{Sig}}^{\text{ON}}(i) - (a_{\text{OFF}} \times \bar{y}_{\text{D},\text{Sig}}^{\text{ON}}(i) + b_{\text{OFF}})\end{aligned}\quad (4)$$

Finally, the HFPNS-corrected barycenter shift  $\Delta y_{\text{HFPNS}}(i)$  for the  $i$ -th ON-OFF measurement is obtained by taking the difference between the corrected prompt barycenters of the ON and OFF intensity profiles:

$$\Delta y_{\text{HFPNS}}(i) = \bar{y}_{\text{PD},\text{Sig}}^{\text{ON}}(i) - \bar{y}_{\text{PD},\text{Sig}}^{\text{OFF}}(i). \quad (5)$$

This approach ensures that common noise between the prompt and delayed pulses is efficiently removed, allowing the extraction of any deflection signal with minimal contamination from the correlated phase fluctuations inside the Sagnac interferometer.

#### D. Expected shot-noise-limited spatial resolution

The spatial resolution limited by shot noise has been experimentally characterized in Ref. [13], using a dedicated test bench with the same CCD camera used in the present HFPNS experiment. In that study, the shot-noise-limited spatial resolution,  $\sigma_y^{\text{SN}}$ , was measured as a function of the peak intensity of the recorded interference beam profile and it is found to be in excellent agreement with corresponding Monte Carlo simulations.

Under the typical operating conditions of the HFPNS setup, the interference signal recorded on the CCD reaches a peak intensity of approximately 1500 ADU. According to the calibration established in Ref. [13], this intensity corresponds to a shot-noise-limited spatial resolution of  $\sigma_y^{\text{SN}} \simeq 36$  nm. In the following, this value is taken as the reference shot-noise level.

## IV. RESULTS

### A. HFPNS Procedure

For the measurements presented in this article, the pump beam is absent. Consequently, the average value  $\langle \Delta y(i) \rangle$  of the signal is expected to be zero since there is no interaction between the pump and probe pulses, and the standard deviation of the barycenter signal distribution  $\sigma_{\Delta y(i)}$  corresponds to the spatial resolution achieved with the HFPNS setup.

The purpose of these measurements is twofold: first, to validate the performance of the HFPNS method, and second, to identify and characterize the remaining sources

of residual phase noise that are not corrected by the system — in particular, the mechanical vibrations induced by the delay stage separating the prompt and delayed pulses.

We present here the measurement of the spatial resolution, obtained with 3500 successive laser shots (at a 10 Hz repetition rate). Data of successive odd and even laser shots are arbitrarily separated into OFF and ON data in order to define  $i$ -th "ON-OFF" measurement at 5 Hz repetition rate. The raw vertical barycenters of the interference intensity profiles of the prompt ( $\bar{y}_{\text{P}}^{\text{ON}}(i)$  and  $\bar{y}_{\text{P}}^{\text{OFF}}(i)$ ) and delay ( $\bar{y}_{\text{D}}^{\text{ON}}(i)$  and  $\bar{y}_{\text{D}}^{\text{OFF}}(i)$ ) are computed within a ROI size equal to the full width at half maximum ( $w_{\text{FWHM}}$ ) of the transverse intensity profile. The distributions of the calculated raw barycenters are presented in Figure 4, showing large fluctuations of the order of few tens of micrometers.

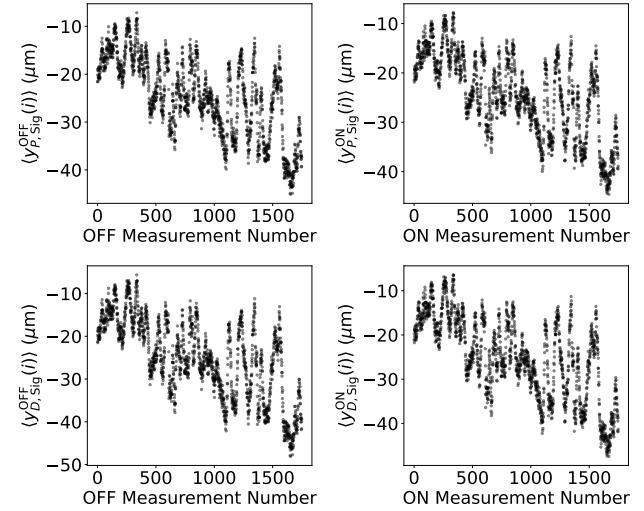


Figure 4. The measured barycenters of the interference intensity profiles within a square analysis window of size  $w_{\text{ROI}} = w_{\text{FWHM}}$  for the prompt (upper plots) and delayed (bottom plots) beams, and for the OFF events (left plots) and the ON events (right plots). In all cases, a slow correlated temporal drift is clearly observed across all the measurement sequence.

Applying direct subtraction between successive ON and OFF measurements, yields the standard ON-OFF signal

$$\Delta y_{\text{Standard}}(i) = \bar{y}_{\text{P},\text{Sig}}^{\text{ON}}(i) - \bar{y}_{\text{P},\text{Sig}}^{\text{OFF}}(i) \quad (6)$$

The resulting distribution is presented in Figure 5 showing that the slow temporal drift is removed. However, large fluctuations ( $\sigma_y^{\text{Standard}} = 1.7 \mu\text{m}$ ) still remain, dominated partly by the beam-pointing instabilities and more importantly by interferometric phase noise.

To suppress the dominant noise contributions in the raw barycenter signals of the prompt pulse, the barycenter correlation between prompt and delay beams is used. Figure 6 shows this correlation for the ON and OFF

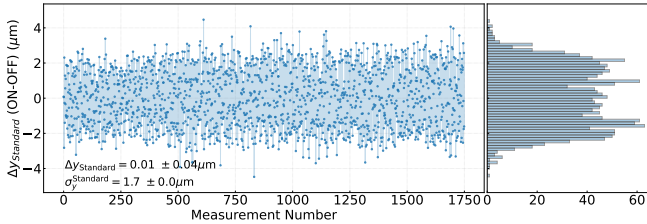


Figure 5. Distribution of the standard ON-OFF signal  $\Delta y_{\text{Standard}}$ , obtained with direct subtraction between successive ON and OFF barycenter measurements of the interference intensity profile, applied on a sample dataset with 3500 successive laser shots at 10 Hz, corresponding to 1750 ON-OFF measurements. The right panel shows the fitted Gaussian distribution on the obtained data.

datasets separately, with linear fits obtained by Eq. (4). A clear linear dependence emerges between the prompt and delayed signals in both cases confirming both signals are similarly affected by common noise sources, such as beam-pointing fluctuations and interferometric phase noise. The fitted linear correlation is then used to suppress the noise from the prompt beam, using Eq. (4). The HFPNS corrected signal  $\Delta y^{\text{HFPNS}}(i)$  is then calculated, following Eq. (5). Note that the fitted parameter  $a_{\text{OFF}}$  is not exactly equal to 1, due to the difference in the optical pathlength between the prompt and delay beams after having been separated by the polarised cube PBS (see Figure 2).

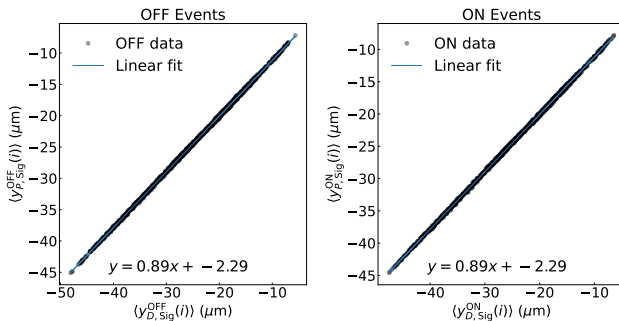


Figure 6. Linear correlation of the barycenters of the intensity profile of the prompt signal  $\bar{y}_P$  vs the delay signal  $\bar{y}_D$  calculated along the vertical  $y$  axis. The data are represented by the black points for both "OFF" (left) and "ON" (right) events. The linear fit obtained by only the OFF events are shown as blue line in both panels.

The resulting distribution of the HFPNS-corrected ON-OFF signal  $\Delta y_{\text{HFPNS}}(i)$  is shown in Figure 7. The gaussian fit of the  $\Delta y_{\text{HFPNS}}(i)$  distribution over all the data collection exhibits an excellent spatial resolution, with  $\sigma_y^{\text{HFPNS}} = 74$  nm. Compared to the dispersion of the standard ON-OFF signal  $\Delta y_{\text{standard}}(i)$  distribution, it corresponds to an improvement by a factor of 28. However, the resulting spatial resolution is about two times

larger than the expected shot noise limited resolution.

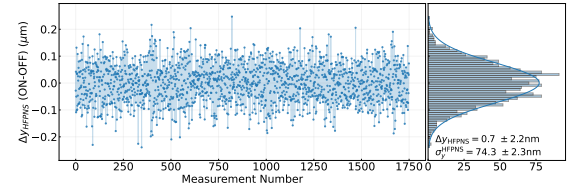


Figure 7. Distribution of the HFPNS ON-OFF signal  $\Delta y_{\text{HFPNS}}$ , obtained with the HFPNS correction method of the interference intensity profiles. After HFPNS correction, the achieved spatial resolution is  $\sigma_y^{\text{HFPNS}} = 74.3$  nm, and the average signal is  $\langle \Delta y_{\text{HFPNS}}(i) \rangle = 0.7 \pm 2.2$  nm, compatible with the expected zero value in the absence of pump pulses.

## B. Residual Noise

The discrepancy between the expected shot noise and the HFPNS-corrected result, referred to as residual noise, is most likely induced by relative difference in the optical path of the prompt and delayed beams, or by instabilities in the delay line both of which can distort the relative intensity profiles prior to their injection into the interferometer. In particular, the delay line used to generate the delayed pulse before entering in the Sagnac interferometer is sensitive to mechanical vibrations, thereby introducing relative fluctuations between prompt and delay signals.

For the further analysis this residual noise, we investigate the Fourier transformation of the HFPNS-corrected barycenter signal. The resulting power spectrum density (PSD) is shown in Figure 8. Two clear resonance peaks are observed in the spectrum at distinct frequencies, which are attributed to mechanical instabilities of the delay line. As discussed in the conclusion, while ongoing efforts aim to improve the mechanical stabilization of the delay stage, these relative noise contributions can also be suppressed at the analysis level.

In this work, we study two approaches for this purpose: the use of back-reflection signals as an auxiliary reference, and the application of passive numerical filtering to the corrected barycenter signal.

## C. Suppression of the residual noise by using back reflections

As explained in Section III, back reflection spots provide the exact replica of the incident beam. Since they propagate along the same optical path as their corresponding interference signals, the prompt and delayed beams, they carry all beam-pointing fluctuations originating from environmental perturbations and optical elements along the beam line, including those induced by the delay line.

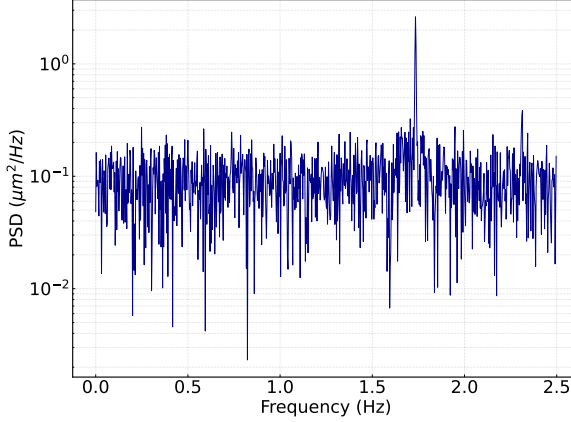


Figure 8. The Power Spectrum Density (PSD) of the HFPNS-corrected interference signal barycenter measurements in logarithmic scale. Two resonance peaks at  $f_1 = 1.733$  Hz and  $f_2 = 2.313$  Hz clearly seen in the spectrum.

From this perspective, we apply the same HFPNS correction method to the prompt and delay direct back reflection spots, using Eq. (4) applied to the barycenters of the prompt and delay back reflection intensity profile. This procedure yields the prompt–delay (PD) corrected back-reflection barycenter measurements, denoted as  $\bar{y}_{PD,Sig,BR}^{OFF}(i)$ , and  $\bar{y}_{PD,BR1}^{ON}(i)$  for the OFF and ON events, respectively. As shown in Figure 9, a clear linear correlation is then observed between the prompt–delay corrected barycenters of the interference intensity profiles and back-reflection intensity profiles. This correlation directly results from the relative fluctuations between the prompt and delay beam, induced by the residual delay line vibrations. This residual noise is then removed by a linear regression procedure defined with the OFF measurements and applied both for the ON and OFF measurements, given by:

$$\begin{aligned} \bar{y}_{PD,Sig,BR}^{OFF}(i) &= \bar{y}_{PD,Sig}^{OFF}(i) - \\ &\quad (\alpha_{OFF} \times \bar{y}_{PD,BR}^{OFF}(i) + \beta_{OFF}) \\ \bar{y}_{PD,Sig,BR}^{ON}(i) &= \bar{y}_{PD,Sig}^{ON}(i) - \\ &\quad (\alpha_{OFF} \times \bar{y}_{PD,BR}^{ON}(i) + \beta_{OFF}) \end{aligned} \quad (7)$$

Finally, the complete HFPNS-corrected signal for the  $i$ -th ON–OFF measurement,  $\Delta y_{HFPNS}^{Comp}(i)$ , is obtained after applying ON–OFF subtraction, given by:

$$\Delta y_{HFPNS}^{Comp}(i) = \bar{y}_{PD,Sig,BR}^{ON}(i) - \bar{y}_{PD,Sig,BR}^{OFF}(i) \quad (8)$$

The distribution of  $\Delta y_{HFPNS}^{Comp}(i)$  is presented in Figure 9. The Gaussian fit gives a spatial resolution of  $\sigma_{y,HFPNS}^{Comp} = 43.9 \pm 1.3$  nm. The result is in agreement with the expected shot noise  $\sigma_{MC} = 44.2 \pm 0.6$  nm, calculated by the Monte-Carlo simulation, when considering the addition of extra back-reflection corrections and

in the presence of delay stage fluctuation with 100  $nrad$  rms. The frequency spectrum of  $\Delta y_{HFPNS}^{Comp}(i)$ , shown in Figure 10, is stable, indicating that the residual noise is purely stochastic as expected for the quantum shot noise of the CCD camera.

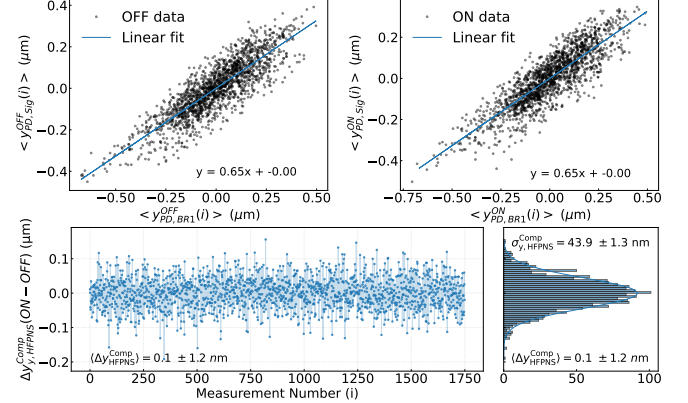


Figure 9. (Upper plots) The residual correlation between the prompt–delay corrected interference signal and back reflections for OFF and ON measurements. The blue curve represents linear fit obtained from the OFF data. (Lower plot) The resulting distribution of the interference signal after HFPNS correction coupled with back reflection correction. Gaussian fit gives the spatial resolution  $\sigma_{y,HFPNS}^{Comp} = 43.9 \pm 1.3$  nm.

The shot noise limit is reached when using extra back reflection corrections. However, as explained in [13], the DeLLight experiment requires to operate with suppressed back-reflections. Indeed, both a small waist of the probe beam at focus and a relatively large focal length are both needed to reach a high sensitivity of detection. This requires to operate with a large diameter for the probe beam circulating in the interferometer, and consequently on the beamsplitter. As also discussed in [13], a relatively thin beamsplitter is also needed. Therefore, in this configuration, the back reflection spots would overlap with the interference signal and consequently would degrade the barycenter measurement. For these reasons, the back reflections must be suppressed in the final setup, by using a beam splitter with an enhanced anti-reflective coating. Consequently, only the prompt and delay interference signals will be displayed in the dark output, and we must define an alternative method to reject the residual noise.

#### D. Suppression of the residual noise by using a passive Notch Filter

Instead of using back reflection spots, we propose here to reject the residual noise by using a numerical notch filter. Recalling the Fourier spectrum of the HFPNS-corrected interference signal shown in Figure 11(a), two pronounced resonance peaks are observed. This spectral feature is attributed to mechanical instabilities of the delay line and motivate the use of a dedicated notch-

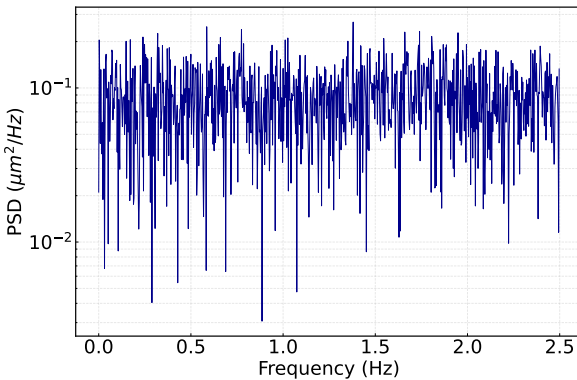


Figure 10. The PSD of the interference signal obtained by the HFPNS method with back reflection. No resonance peak is observed after the additional back reflection correction.

filtering approach to suppress this noise contribution in the absence of back-reflection signals.

For this purpose, in the analysis procedure, a passive notch filter targeting the two resonance frequencies at  $f_1 = 1.733$  Hz and  $f_2 = 2.313$  Hz is applied on the HFPNS corrected interference signal. The phase response of this implemented notch filters at these two frequencies is shown in Figure 11(b). By attenuating these narrow-band noise contributions selectively, the filter effectively suppresses the noise resonances without affecting the broadband noise floor or biasing a potential signal. It is further validated through Monte Carlo simulations performed on a synthetic dataset with comparable intensity, in which barycenter fluctuations are artificially injected at the same resonance frequencies.

The resulting Fourier transform of the HFPNS corrected barycenter signal after notch filtering is presented in Figure 11(c). A clear suppression of the spectral peaks at  $f_1$  and  $f_2$  is observed, confirming the efficiency of the filtering procedure, without changing the PSD of the flat background white noise.

With the notch filter, we obtain the final distribution of the interference barycenter measurement as shown in Figure 12, represented by the red data points. A Gaussian fit to this distribution yields a spatial resolution of  $\sigma_y = 45.9 \pm 0.5$  nm. It is only 1.3 times higher than the Monte-Carlo expected quantum-noise-limited spatial resolution of 36 nm, and indicates that the dominant interferometric phase noise and other sources of noise have been effectively suppressed by the HFPNS method coupled with a numerical notch filter. The average signal is  $\langle \Delta y(i) \rangle = -0.5 \pm 0.5$  nm, which is compatible with the expected zero value in the absence of pump pulses.

### E. Efficiency of HFPNS Method

The capacity to measure the displacement of the barycenter of the intensity profile depends on the ROI

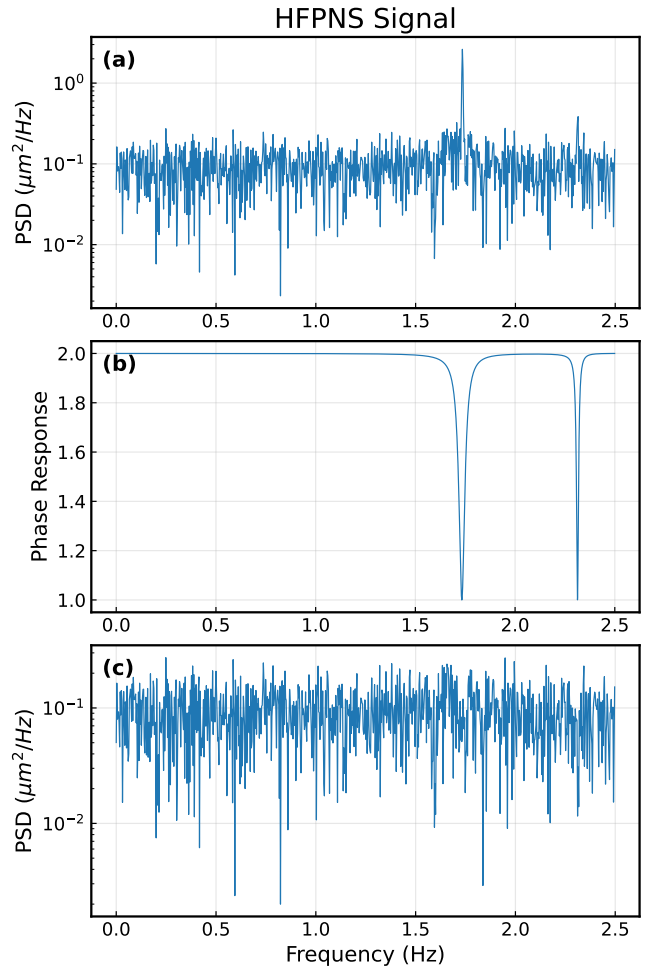


Figure 11. (a) The Power Spectrum Density (PSD) of the HFPNS corrected barycenter of interference obtained by Discrete Fourier Transformation. Two resonance peaks at  $f_1 = 1.733$  Hz and  $f_2 = 2.313$  Hz appear. (b) The phase response of the numerical notch filter designed to the same resonance frequencies. (c) The PSD of the signal after applying the corresponding notch filter.

size of the analysis window. We define the efficiency  $\epsilon_s(RoI)$  as the ratio between the barycenter shift measured within a given RoI size and the true barycenter shift of the full beam profile. The theoretical efficiency curve, calculated for a Gaussian transverse profile of the beam, is presented in Figure 13, as a function of the RoI size. The efficiency increases with the window size and asymptotically approaches 1 as it becomes large enough to include the entire beam, i.e.  $\epsilon_s = 1$  as  $w_{RoI} = \infty$ .

However, the spatial resolution is strongly degraded when the RoI size is increased because the influence of the interferometric phase noise increases highly with the RoI size, as studied in [13].

Figure 14 shows the measured spatial resolution, as a function of the RoI size (given in FWHM unit), for five different analysis methods: standard ON-OFF subtraction (blue), HFPNS method (orange), and HFPNS

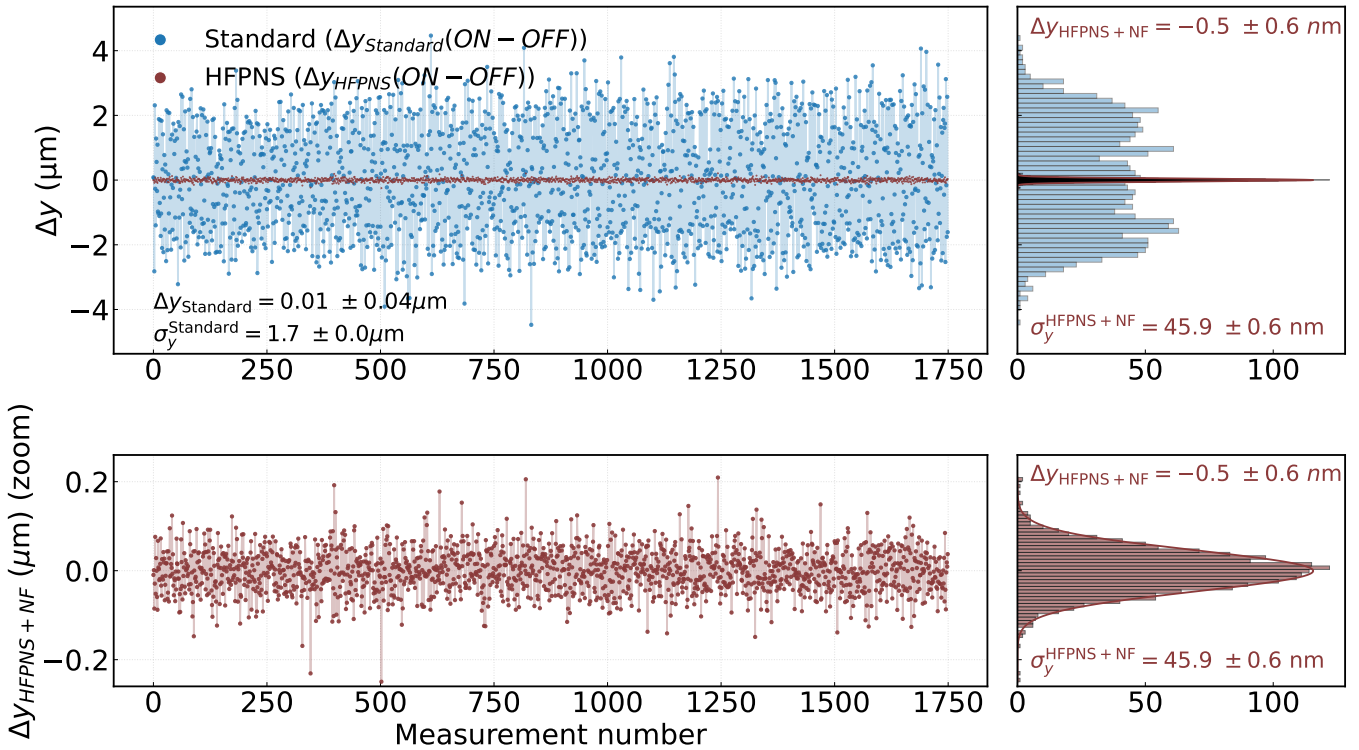


Figure 12. Same as Figure 7 but, in red, after applying the HFPNS correction and the numerical Notch filter. After HFPNS and Notch filter corrections, the achieved spatial resolution is  $\sigma_{\text{HFPNS}} = 45.9 \text{ nm}$ , and the average signal is  $\langle \Delta y(i) \rangle = 0.5 \pm 0.5 \text{ nm}$ , which is compatible with the expected zero value in the absence of pump pulses.

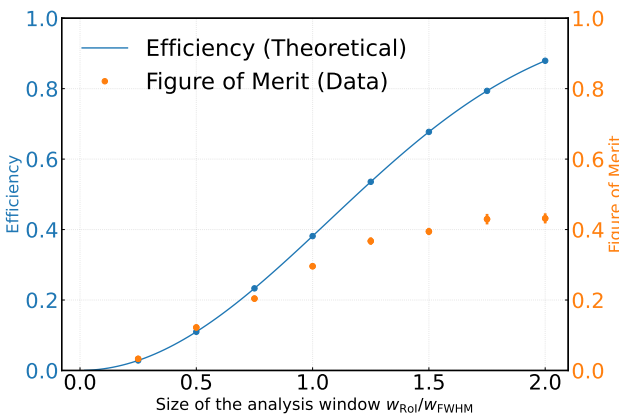


Figure 13. The theoretical efficiency  $\epsilon_s$  (blue curve) and the measured figure of merit  $\xi$  (orange dots) as a function of the ROI size normalized with the FWHM of the Gaussian beam profile.

method with the use of back reflection (green), HFPNS method with notch filter (red), and finally the Monte Carlo shot noise simulation (violet).

With the standard ON-OFF subtraction, the spatial resolution is strongly degraded as the ROI size is increased, reaching the micrometer scale. This behavior

demonstrates the dominance of beam-pointing fluctuations and above all interferometric phase noise, which are not sufficiently suppressed by the ON-OFF procedure and become increasingly dominant in larger window sizes.

In contrast, the HFPNS method result shows significantly improved and more stable spatial resolution over the full range of ROI sizes. The suppression of correlated noise through the prompt–delay correlation leads to a resolution that closely follows the Monte Carlo shot-noise prediction, especially for ROI sizes around the beam FWHM size.

The results obtained with the additional correction by using back reflection (HFPNS+BR), and applying a passive notch filter to suppress relative peaked noise (HFPNS+NF), indicate that noise contributions which are not directly addressed by the HFPNS method can also be effectively removed. As a result, the measurement sensitivity approaches the ultimate shot-noise limit. This clearly demonstrates that the HFPNS method provides a robust, near shot-noise-limited spatial sensitivity that is weakly dependent on the choice of analysis window size.

Finally, to identify the optimum analysis window (ROI) size for the barycenter measurement, we introduce the figure of merit,  $\xi$ , defined as the product of the efficiency and the ratio between the shot-noise-limited spatial resolution and the experimentally measured spatial resolu-

## V. CONCLUSION

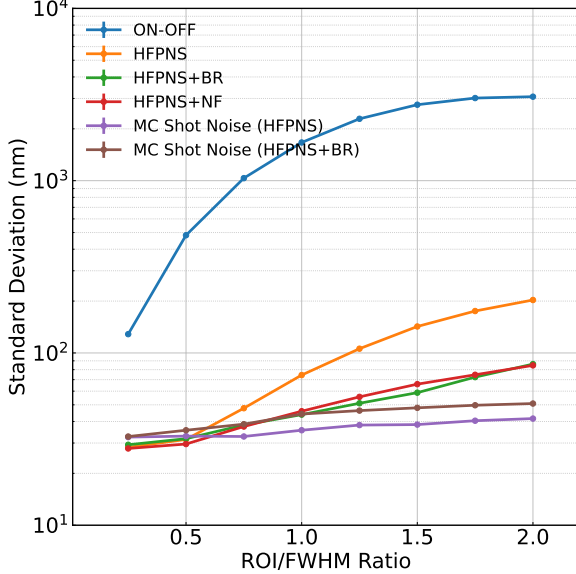


Figure 14. Spatial resolution as a function of the RoI size in fraction of the beam FWHM for different analysis procedures: the blue curve corresponds to the standard ON-OFF subtraction of the interference signal barycenter. The orange curve shows the HFPNS correction applied only on the interference signal while the green and red curves are representing the complete HFPNS correction using the correlations of the back reflection and adding a notch filter, respectively. Finally, the violet and brown curves indicate the expected shot noise limits obtained by the Monte Carlo simulation with the use of back reflection spots and with notch filter, respectively.

tion, and given by

$$\xi = \epsilon_s \times \frac{\sigma_{\text{shot noise}}}{\sigma_{\text{measured}}} \quad (9)$$

This parameter accounts for the signal detection efficiency and noise performance. For the data presented in this article, the measured figure of merit is also presented in Figure 13 as a function of the RoI size. It reaches a maximum value of  $\xi = 0.44$  for an optimal analysis window size  $w_{RoI} = 1.75 \times w_{FWHM}$ , where  $\epsilon_s = 0.8$  and  $\sigma_y = 75$  nm. It corresponds to an achieved sensitivity that is 2.3 times higher than the ultimate sensitivity.

The results presented in this article confirm the capability of the HFPNS method to suppress the phase noise arising from fluctuations in the interferometric optics effectively. The method involves introducing a delayed replica of the probe pulse that carries identical noise characteristics, and exploiting the strong linear correlation between the barycenter fluctuations of both pulses. This approach enables efficient noise suppression without compromising the integrity of a potential signal. After applying this method on a sample dataset, the spatial resolution obtained,  $\sigma_y = 45.9 \pm 0.5$  nm, is close to the CCD camera's shot-noise limit, around 36 nm, demonstrating that most of the correlated phase noise has been successfully suppressed. Including the efficiency to measure entirely the lateral shift in the intensity profile of the interference signal induced by deflection, which depends on the size of the analysis window, the sensitivity obtained here is a factor 2.3 higher than the ultimate sensitivity.

The presence of residual uncorrelated noise indicates that certain noise components are not fully measured and subtracted by the current suppression scheme. Control measurements based on the back-reflection intensity profiles support this conclusion, revealing persistent discrepancies between the prompt and delayed beams that likely arise from optical asymmetries or additional fluctuations along the delay path.

Complementary stabilization techniques or enhanced correction methods, such as optimized notch filtering, may be required to ultimately achieve quantum-limited sensitivity in future implementations. To further enhance the performance of the detection system, several improvements are considered. First, implementing a more advanced notch filtering strategy will allow more efficient isolation and suppression of specific low-frequency noise components. Second, mechanical stabilization of the delay line will be improved to minimize differential fluctuations between the two pulses. Finally, employing a CCD camera with a higher charge storage capacity per unit surface, will make it possible to reach the target spatial resolution required for detecting the expected QED-induced deflection signal and to reveal the QED predicted optical non linearity of the quantum vacuum.

---

[1] H. Euler and B. Kockel, Über die streuung von licht an licht nach der diracschen theorie, *Naturwissenschaften* **23**, 246 (1935).

[2] W. Heisenberg and H. Euler, Folgerungen aus der diracschen theorie des positrons, *Zeitschrift für Physik* **98**, 714 (1936).

[3] J. Schwinger, On gauge invariance and vacuum polarization, *Physical Review* **82**, 664 (1951).

[4] D. Burke, R. Field, G. Horton-Smith, J. Spencer, D. Walz, S. Berridge, W. Bugg, K. Shmakov, A. Weidemann, C. Bula, and others., Positron production in multi-photon light-by-light scattering, *Physical Review Letters* **79**, 1626 (1997).

[5] ATLAS Collaboration, Evidence for light-by-light scattering in heavy-ion collisions with the atlas detector at the lhc, *Nature physics* **13**, 852 (2017).

[6] A. M. Sirunyan, A. Tumasyan, W. Adam, F. Ambrogi, E. Asilar, T. Bergauer, J. Brandstetter, M. Dragicevic, J. Erö, A. E. Del Valle, and others., Evidence for light-by-light scattering and searches for axion-like particles in ultraperipheral pbpb collisions at  $s_{\text{NN}} = 5.02$  tev, Physics Letters B **797**, 134826 (2019).

[7] S.-J. Chen, H.-H. Mei, and W.-T. Ni, Q & a experiment to search for vacuum dichroism, pseudoscalar–photon interaction and millicharged fermions, Modern Physics Letters A **22**, 2815 (2007).

[8] X. Fan, S. Kamioka, T. Inada, *et al.*, The oval experiment: a new experiment to measure vacuum magnetic birefringence using high repetition pulsed magnets, Eur. Phys. J. D **71**, 10.1140/epjd/e2017-80290-7 (2017).

[9] A. Ejlli, F. Della Valle, U. Gastaldi, G. Messineo, R. Pengo, G. Ruoso, and G. Zavattini, The pvlas experiment: A 25 year effort to measure vacuum magnetic birefringence, Physics Reports **871**, 1 (2020), the PVLAS experiment: A 25 year effort to measure vacuum magnetic birefringence.

[10] Zavattini, Guido, Della Valle, Federico, Soflau, Alina Mariana, Formaggio, Lorenzo, Crapulli, Giacomo, Messineo, Giuseppe, Mariotti, Emilio, Kunc, Štefan, Ejlli, Aldo, Ruoso, Giuseppe, Marinelli, Carmela, and An-dreotti, Mirco, Polarimetry for measuring the vacuum magnetic birefringence with quasi-static fields: a systematics study for the vmb@cern experiment, Eur. Phys. J. C **82**, 159 (2022).

[11] D. Xu, B. Shen, J. Xu, and Z. Liang, Xfel beamline design for vacuum birefringence experiment, Nuclear Instruments and Methods in Physics Research Section A: Accelerators, Spectrometers, Detectors and Associated Equipment **982**, 164553 (2020).

[12] A. E. Kraych, A. M. Mailliet, F. m. c. Couchot, X. Sarazin, E. Baynard, J. Demaily, M. Pittman, A. Djannati-Ataï, S. Kazamias, S. Robertson, and M. Urban, Interferometric measurement of the deflection of light by light in air, Phys. Rev. A **109**, 053510 (2024).

[13] A. M. Mailliet, A. E. Kraych, F. Couchot, X. Sarazin, E. Baynard, J. Demaily, M. Pittman, A. Djannati-Ataï, S. Kazamias, S. Robertson, and M. Urban, Performance of a sagnac interferometer to observe vacuum optical non-linearity (2024), arXiv:2401.13720 [physics.optics].

[14] S. Robertson, A. Mailliet, X. Sarazin, F. m. c. Couchot, E. Baynard, J. Demaily, M. Pittman, A. Djannati-Ataï, S. Kazamias, and M. Urban, Experiment to observe an optically induced change of the vacuum index, Phys. Rev. A **103**, 023524 (2021).